High-resolution spectroscopy of Rydberg states in an ultracold cesium gas

H. Saßmannshausen, F. Merkt, and J. Deiglmayr*
Laboratory of Physical Chemistry, ETH Zurich, Switzerland
(Received 23 January 2013; published 27 March 2013)

Transitions between high Rydberg states of ^{133}Cs atoms have been studied by high-resolution millimeter-wave spectroscopy of an ultracold sample. The spectroscopic measurements were performed after releasing the atoms from a magneto-optical trap. Switching off all trapping fields and compensating the stray electric and magnetic fields to below 1 mV/cm and 2 mG, respectively, prior to the spectroscopic measurement enabled the recording of millimeter-wave spectra of Rydberg states with principal quantum number beyond $n = 100$ under conditions where the inhomogeneous broadening by stray fields is minimal and no dephasing of the Rydberg-atom sample can be detected over measurement times up to 60 μs. The Fourier-transform-limited line widths of better than 20 kHz enabled the observation of the hyperfine structure of nS and nP Rydberg states of Cs beyond $n = 90$. The analysis of the line shapes of transitions to Rydberg states with $n \approx 230$ indicated that field inhomogeneities across the atomic sample represent the dominant cause of spectral broadening at high n values. The analysis also revealed that the initial polarization of the atomic sample ($F = 4$, $M_F = 4$) is preserved for several tens of microseconds, the depolarization being caused by slow precession along the magnetic stray fields.

DOI: 10.1103/PhysRevA.87.032519 PACS number(s): 32.30.−r, 32.80.Ee, 37.10.Gh, 32.70.Jz

I. INTRODUCTION

This article describes a spectroscopic study of very high Rydberg states of ^{133}Cs in a magneto-optical trap (MOT) under conditions where Doppler broadening and line broadening caused by the finite transit time of the atoms in the measurement region are negligible. The residual line broadening is exclusively caused by residual stray electric and magnetic fields and by transitions induced by blackbody radiation. Under these conditions, we demonstrate that it is possible to resolve Rydberg series, including their hyperfine structures, up to high values of the principal quantum number. It is also possible to quantify the effects of weak electric and magnetic fields on the spectral structures.

High Rydberg states are electronically highly excited states that can be regarded, in first approximation, as consisting of a positively charged ion core weakly interacting with a distant electron in an orbital of high principal quantum number n. These states form series that can be described by Rydberg's formula

$$\nu_n = E_{\mathrm{I}}^{\alpha^+}/h - cR_M/(n-\delta)^2. \quad (1)$$

In Eq. (1), ν_n represents the spectral position of the Rydberg states in frequency units, $E_{\mathrm{I}}^{\alpha^+}$ the convergence limit of the series, which represents the energy required to form an ion in quantum state α^+, R_M the mass-dependent Rydberg constant ($R_M = R_\infty M^+/(m_e + M^+)$; m_e and M^+ are the masses of the electron and ion core, respectively), c is the speed of light in vacuum and δ is the quantum defect. Most physical properties of Rydberg states scale as integer powers of n, e.g., their lifetime as n^3, their polarizability as n^7, the threshold field for field ionization as n^{-4}, and the van der Waals interaction between a pair of Rydberg atoms as n^{11} [1,2]. The weakly bound nature of the Rydberg electron and the resulting high sensitivity of high Rydberg states to their environment are simultaneously a curse and a blessing: A blessing, because it is the origin of most applications of high Rydberg states, and a curse because artifacts can easily mask the effects one desires to study. For instance, the presence of only a few ions in the measurement volume can alter the line shapes and line positions in spectra of high Rydberg states [3,4], which in turn may be interpreted as arising from other effects. Thus in the spectroscopy of Rydberg states a thorough investigation of all line-broadening mechanisms is required.

The high Rydberg states of ^{133}Cs have been extensively characterized by O'Sullivan and Stoicheff [5], Lorenzen and Niemax [6], and Weber and Sansonetti [7], who employed optical two-photon spectroscopy to obtain quantum defects and selected fine and hyperfine structure intervals for the nS, nP, nD, nF, and nG series of neutral cesium reaching up to $n \approx 80$. The hyperfine structure of Rydberg states of cesium has attracted interest since the early days of high-resolution spectroscopy, both as test bed for new spectroscopic methods and as tests of atomic-structure calculations (the early work on Rydberg states with $n < 20$ is reviewed by Arimondo *et al.* [8]).

Goy *et al.* [9] used millimeter-wave spectroscopy to investigate Rydberg transitions in an atomic beam of cesium, reporting hyperfine splittings for $nS_{1/2}$ and $nP_{1/2}$ states up to $n = 28$. In comparison to the optical spectroscopy of transitions to Rydberg states, the spectroscopy of transitions between Rydberg states using microwave frequencies benefits from the reduced Doppler shift at lower frequencies and the availability of narrow-line-width (<1 kHz) sources for frequencies up to few hundred GHz [10]. In beam experiments transit-time-limited line widths of 60 kHz have been achieved [3]. The lifetime-limited natural line width of Rydberg states can, however, be much narrower than 1 kHz [2]. Intrinsic line broadening, if not caused by the fine and hyperfine structures, arises in Rydberg samples either as a result of the Stark and Zeeman effects or as a result of interactions of the Rydberg atoms with neighboring atoms. The full interpretation of high-resolution spectra necessitates disentangling these sources of spectral broadening, i.e., to perform a careful characterization of the influence of external fields on the spectral features at densities sufficiently low that interparticle interactions play no

*jdeiglma@ethz.ch

role. In beam experiments, external electric and magnetic fields can be strongly reduced by enclosing the interaction region with conducting and highly magnetic-permeable shields, respectively. Using such measures residual electric fields as low as 50 μV/cm may be obtained [3,11,12].

Several applications of Rydberg atoms, such as the realization of the excitation blockade mechanism of interest in quantum information science [13,14], rely on the generation and use of dense Rydberg atom samples at very low temperatures, usually alkali-metal atoms in MOTs, which offer experimental conditions under which Doppler broadening and transit-time broadening are negligible. The operation of a MOT requires good optical access to the interaction region, which prevents rigorous shielding of external fields. Thus the compensation of stray electric and magnetic fields in MOTs to a level where they do not affect the spectral properties of high Rydberg states is a challenging task. Nevertheless residual electric fields as low as 1 mV/cm have been reported using active field cancellation [15]. By choosing transitions between states with a small differential shift in a magnetic field, Li *et al*. obtained millimeter-wave spectra with line widths as low as 100 kHz, even in the presence of the strong magnetic field gradient required for the operation of a MOT [16]. The present article demonstrates how electric and magnetic stray fields can be reduced to below 1 mV/cm and 2 mG, respectively, enabling measurements of the hyperfine structures of Cs Rydberg atoms at much higher n values than in earlier works.

The article is organized as follows: The experimental setup is described in Sec. II and Sec. III presents the experimental procedures used for Rydberg-state excitation and detection and for stray-field compensation. The results of the measurements of the hyperfine structure of high-n Rydberg states are presented in Sec. IV and the article is concluded with a brief summary.

II. EXPERIMENTAL SETUP

The central element of the experimental setup is a MOT for cesium atoms. The optical layout is shown schematically in Fig. 1(a). The main source of narrow-band laser light at 852.3 nm is a master-oscillator power-amplifier (MOPA) system. Repumping light is provided by an additional external-cavity diode laser. Variable beam splitters and acousto-optical modulators (AOMs) are used to generate intensity- and frequency-controlled light from these two lasers. The light for laser cooling is detuned by $\approx$2.8 Γ from the $6S_{1/2}$, $F = 4 \rightarrow 6P_{3/2}, F' = 5$ transition and is split into three beams with roughly equal intensities which are coupled into three polarization-maintaining single-mode fibers. The repumping light is resonant with the $6S_{1/2}, F = 3 \rightarrow 6P_{3/2}, F' = 4$ transition. It is spatially overlapped with the two beams used for cooling in the horizontal plane and is coupled into the same fibers. Before traversing the vacuum chamber along three mutually orthogonal optical axes, the three laser beams are coupled out of the fibers, expanded to a diameter of roughly 20 mm, and changed to circular polarization by quarter-wave plates. The beams are retro reflected outside of the vacuum chamber.

The magnetic-field gradient for the MOT is produced by a pair of coils in an anti-Helmholtz configuration. Each coil consists of 35 windings of copper band (width 15 mm, thickness 0.45 mm) with a mean radius of 53 mm. The coils are mounted at a distance of 65 mm from each other outside of the vacuum chamber in reentrant view ports. To produce a

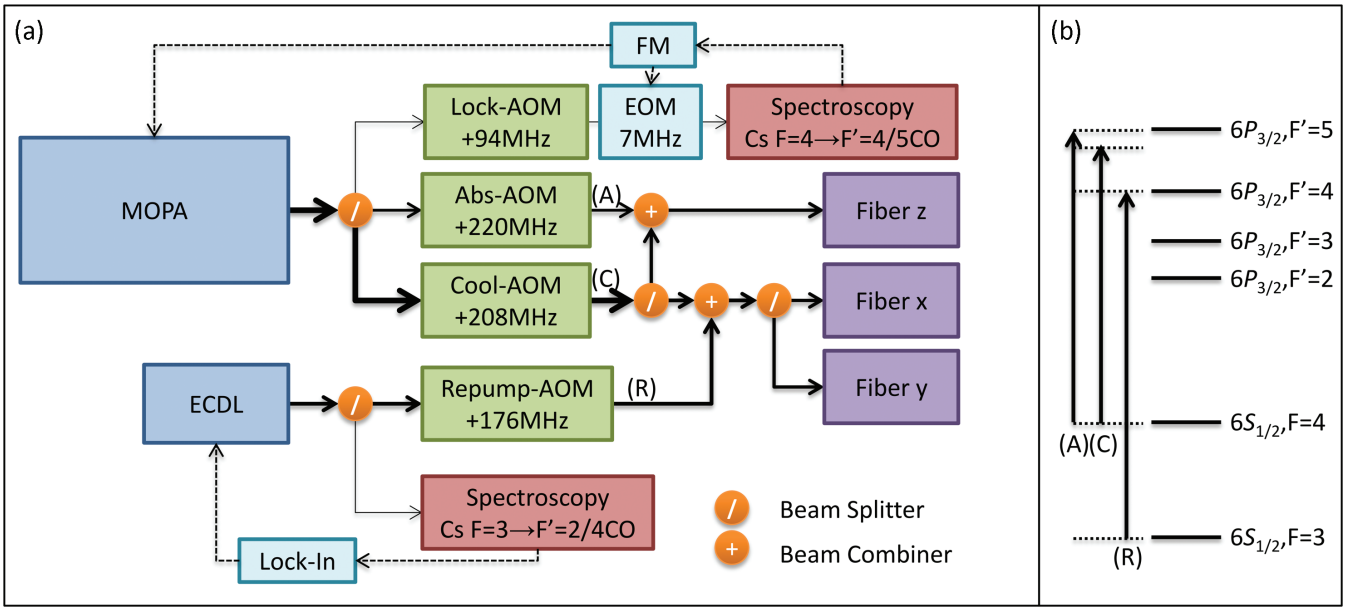

FIG. 1. (Color online) (a) Schematic overview of the laser setup for laser cooling of cesium. The frequency of the master-oscillator power-amplifier (MOPA) system (Toptica TA-Pro) is stabilized by frequency-modulation (FM) spectroscopy [17] of a saturated absorption line of atomic cesium. The frequency modulation of the laser light required for the FM scheme is performed by a resonantly driven electro-optical modulator (EOM). Repumping light is provided by an external-cavity diode laser (ECDL, Toptica DL-Pro), which is stabilized to a second saturated absorption line of cesium atoms using a lock-in detection scheme. (b) Overview of the relevant transitions coupling the hyperfine components F of $6S_{1/2}$ and F' of $6P_{3/2}$: (A) light for absorption imaging, (C) light for laser cooling, (R) light for repumping.

gradient of 10.5 G/cm, a current of 8.0 A is passed through the coils.

Cesium atoms are provided by high-purity resistively heated dispensers (Alvasource AS-3-Cs-100-F) placed at a distance of roughly 15 cm from the MOT. The MOT can also be loaded from cesium vapor produced by light-induced atomic desorption (LIAD) [18] of cesium atoms from the walls and view ports of the chamber. The UV light for the LIAD process is produced by three high-power light-emitting diodes (LEDs; Edixeon EDEV-SLC1-R), each emitting approximately 580 mW of light at a central wavelength of 402 nm. The LEDs are installed outside of the vacuum chamber and the light enters the chamber through a fused-silica window. This loading scheme leads to a significant increase in the number of trapped atoms.

A. Absorption imaging

We determine the number, the density, and the temperature of the trapped atoms by absorption imaging of the atom cloud. The radiation for absorption imaging is provided by the master laser and can be independently modulated in frequency and intensity by an AOM. It is overlapped with the cooling laser beam in the vertical direction, and the two light fields are coupled into the fiber with orthogonal polarization. In front of the chamber, these polarizations are converted into left- and right-handed circular polarizations by a quarter-wave plate [see Fig. 2(b) for a schematic drawing]. After the chamber, a combination of a quarter-wave plate and a polarizing-beam-splitter cube is used to separate the two frequency components based on their state of polarization. The plane containing the trapped atoms is imaged by a pair of identical achromatic lenses onto a charge-coupled-device (CCD) chip. The scale of the acquired image was calibrated before the final assembly by imaging a ruler at the position of the MOT. In order to obtain an absorption image, the cooling light is switched off using an AOM, and an exposure of the CCD chip is triggered. Then the absorption light is switched on for about 100 μs, and the image of the atom cloud is read out digitally and processed by software. All timing sequences for controlling the MOT are generated by a DAQ-Card (National Instruments PCI-6259), which is programmed using LabView. The atomic samples used for the spectroscopic measurements described in this article had a typical peak density of 5×10^9 atoms/cm^3, a $1/e$ sample diameter of 150 μm, and a temperature of 10 μK, as determined from the analysis of the absorption images.

B. Electrode geometry

The electrode structure for the manipulation and detection of Rydberg atoms consists of two segmented, ring-shaped electrodes (called "field plates" in the following) spaced by 40 mm and an ion lens for imaging the Cs^+ ions onto a multichannel-plate (MCP) detector. The shape and positions of the elements are indicated in Fig. 2 and were designed for the creation of homogeneous fields at the position of the MOT. Each field plate consists of four electrodes. These electrodes can be used to apply compensation, polarization, or ionization and ion-extraction fields. For the generation of compensation and polarization fields, voltages of a few volts are generated by a computer-controlled DAQ-Card (Measurement Computing USB-3105) and are, after analog filtering and down-scaling by a 1:6 voltage divider, directly applied to the electrodes. The potential configurations used to apply compensation electric fields along the z, x, and y directions are schematically depicted in Fig. 3(a), 3(b), and 3(c), respectively.

Rydberg atoms can be ionized by applying positive high-voltage pulses either to the four field plates on the opposite site of the MCP [see Figs. 2 and 3(c)] or to the ring electrodes in front of the MCP. In the former case, four home-built

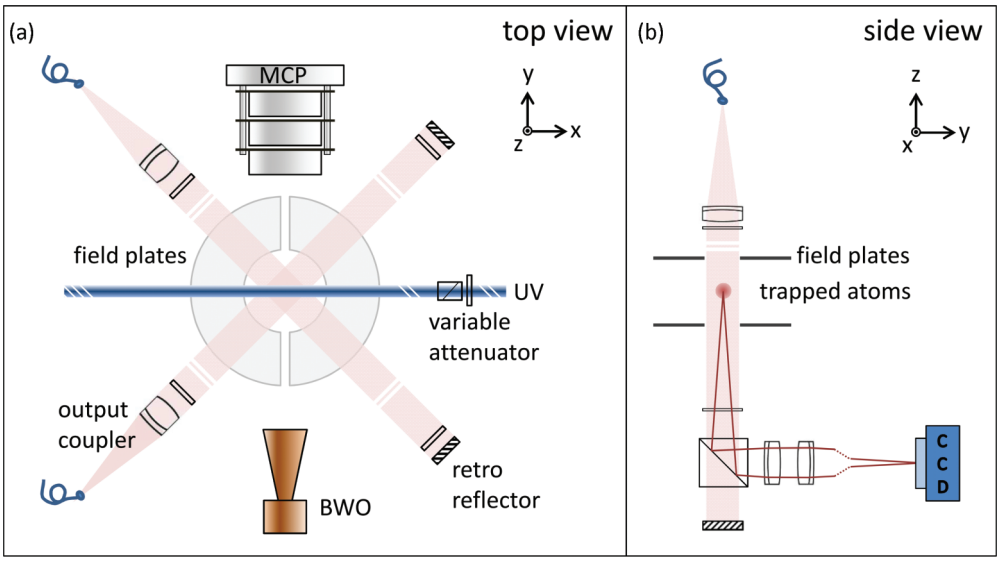

FIG. 2. (Color online) (a) Schematic top view of the setup. Pairs of fiber output couplers and retro reflectors deliver the cooling and repumping light (see text for details). UV light excites ground-state atoms into Rydberg states, and millimeter-wave radiation from a backward-wave oscillator (BWO) drives transitions between Rydberg states. Field plates (see Fig. 3) can be used to apply electric fields across the photoexcitation region. (b) Schematic side view of the setup showing how the atom cloud is imaged onto a charge-coupled-device (CCD) chip by a matched pair of achromatic lenses.

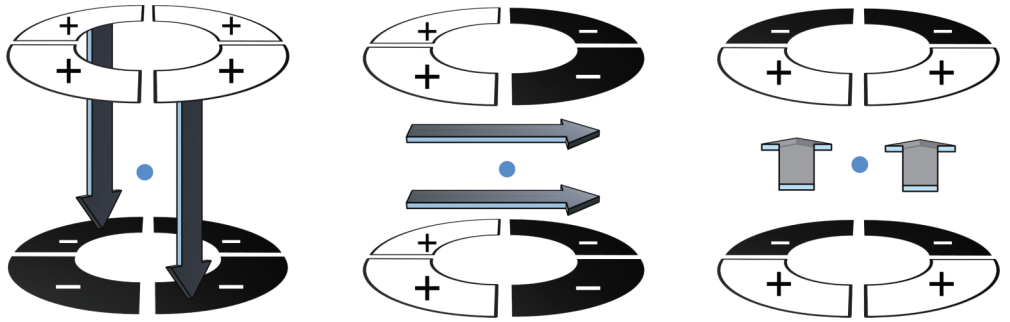

FIG. 3. (Color online) Schematic description of the three potential configurations for the eight electrodes generating homogeneous electric fields at the position of the MOT (blue circle). Electrodes with positive potentials are presented in white and electrodes with a negative potential in black. The arrows indicate the direction of the electric field vectors. The configuration on the left-hand side generates an electric field in z direction, the configuration in the middle generates a field in x direction and the configuration on the right-hand side generates a field in y direction.

high-voltage switches are used to switch from a potential configuration for the compensation of stray electric fields to a potential configuration for the ionization of Rydberg atoms. Applying the high-voltage pulses to the ring electrodes enables one to avoid applying pulsed voltages to the field plates, which reduces transient stray fields in the region where the atom cloud is located. The resulting ionization fields are smaller and only suitable to detect Rydberg states with $n > 50$. Consequently, we apply the ionization-voltage pulses to the ring electrodes to detect Rydberg states with $n > 50$ and to the field plates for the detection of Rydberg states in the range $50 > n > 30$. Electric fields of sufficient strength to field ionize Rydberg states below $n \approx 30$ cannot be generated.

C. Magnetic coils

Three pairs of coils have been installed around the chamber to compensate external magnetic fields or to apply well-defined magnetic fields to the atomic sample. The compensation field in the z direction is produced by a pair of coils in Helmholtz configuration. The coils are wound around the gradient coils of the MOT and consist of 13 copper-band windings with a radius of 67.5 mm located at a distance of 33 mm from the center of the MOT. In the y direction, the coils are mounted on flanges of the vacuum chamber. The coils consist of 64 windings of wire (ribbon cable) with a radius of 57 mm located at a distance of 63 mm from the center of the MOT. Because of the geometry of the chamber, a pair of asymmetric coils is used to apply magnetic fields in the x direction. The first (second) coil consists of 27 windings (150 windings) with a mean radius of 57 mm (78 mm) located at a distance of 100 mm (195 mm) from the center of the MOT. The ratio of the windings of these two coils has been chosen so as to obtain a homogeneous magnetic field at the position of the atom cloud when the same current passes through both coils. The number of windings of all three pairs of coils has been adjusted to generate a magnetic field of about 1 G at the position of the MOT for a current of 1 A through each pair of coils. Under these conditions, a magnetic field variation of ≈0.5 mG results over the 100 μm large atom cloud.

D. Rydberg spectroscopy

A pulsed frequency-doubled dye laser (DCM in ethanol, 0.05 cm^{-1} bandwidth) is used to excite a fraction of the ultracold cesium atoms to a high Rydberg state. The dye laser is pumped by a 10 Hz Nd:YAG laser operated at a wavelength of 532 nm and a pulse energy of ≈70 mJ. After frequency doubling in a BBO crystal, the laser wavelength is centered around 320 nm and can be tuned to induce transitions from the $6S_{1/2}$ electronic ground state of cesium to the Rydberg series converging to the $^1S_0$ ground state of Cs^+. The pulsed UV radiation is linearly polarized along the y axis, and the pulse energy can be adjusted between 5 and 80 μJ/pulse by using an attenuator consisting of a half-wave plate and a UV polarizer.

Spectra of transitions from the initially prepared Rydberg state to higher-lying Rydberg states were recorded with millimeter-wave radiation. As continuous millimeter-wave source, we used the phase-locked backward-wave oscillator (BWO) described in Ref. [10]. Its frequency can be continuously tuned in the range of 240–380 GHz, and its bandwidth is narrower than 1 kHz [10]. The output horn of the BWO is placed 40 cm away from the center of the MOT, and the millimeter-wave radiation intersects the UV-laser beam at right angles (cf. Fig. 2).

The output of the BWO is stabilized in a phase-lock loop to $f_{RF} + Nf_{LO}$, where Nf_{LO} is the Nth harmonic (N = 10–15) of the frequency of a local oscillator (Wiltron 6769B, discontinued product) and f_{RF} is the frequency of an additional radio-frequency (RF) generator (Agilent 8647A, Palo Alto, CA). The output frequency is tuned by changing f_{LO} between 22.8 and 25.1 GHz in minimum frequency steps of 1 kHz. Because the 10th to 15th harmonics of f_{LO} are used for the frequency stabilization, the minimum step size by which the output frequency can be varied is 10–15 kHz, which is too large for the narrowest lines observed in the experiments. As an extension of the performance of this source as compared to the description in Ref. [10], a frequency step size below 1 kHz could be obtained by scanning the frequency f_{RF} of the reference signal (350 MHz in normal operation) instead of f_{LO}. In this way, the frequency step size could be reduced to 1 Hz.

III. EXPERIMENTAL PROCEDURE

A. Photoexcitation

The experiment runs in a pulsed mode at a frequency of 10 Hz given by the repetition rate of the Nd:YAG laser used to pump the dye laser. After a MOT-loading phase of

≈92 ms, the magnetic fields in the MOT are turned off to enable spectroscopy of Rydberg states under field-free conditions. To avoid eddy currents influencing the measurements, the electric currents in the gradient coils are turned off 7.4 ms before application of the laser pulse used to prepare the Rydberg states. After a pseudomolasses phase, the MOT lasers are turned off 400 μs (cooling laser) and 50 μs (repumping laser) before Rydberg excitation to avoid the generation of ions through direct photoionization of atoms in the $6P_{3/2}$ state by a UV photon. Because the cooling laser is turned off before the repumping laser, the cesium atoms are prepared in the $F = 4$ hyperfine component of the $6S_{1/2}$ state. To obtain a purely oriented sample of atoms in the $M_F = 4$ state, the atomic sample is exposed to a beam of circularly polarized laser light propagating along the z direction and resonant with the $6P_{3/2}, F' = 5 \leftarrow 6S_{1/2}, F = 4$ transition for 100 μs. This laser is then turned off 20 μs prior to Rydberg excitation.

Because of a Cooper minimum in the photoexcitation cross section from the $6S_{1/2}$ state to the nP (ϵP) states (continuum) of cesium just above the ionization threshold [19], $nP_{1/2}$ states with $n > 40$ are very difficult to access by one-photon excitation from the electronic ground state. The UV laser pulse energy is adjusted so as to only excite a small fraction, typically less than 10%, of the cesium atoms to a selected $nP_{3/2}$ Rydberg state with n in the range $30 < n < 150$. Under these conditions, the number of atoms excited to Rydberg states remains low, and many-body interactions are negligible. For the measurement of millimeter-wave spectra, the UV laser frequency is kept fixed at the position of a selected $nP_{3/2} \leftarrow 6S_{1/2}, F = 4$ transition. The laser line width of ≈0.05 cm^{-1} enables the excitation of isolated Rydberg states up to $n \approx 140$. All hyperfine transitions allowed by electric-dipole selection rules are excited.

The interaction time of the millimeter-wave radiation and the Rydberg states is determined by the delay time between the UV-laser pulse used for the initial excitation and the application of the electric-field pulse used for detection of the transitions. Because the UV pulse is short compared to this delay time and the electric-field pulse immediately shifts the transitions out of resonance, the effect of the millimeter-wave radiation inducing the Rydberg-Rydberg transitions can be described to a good approximation by a square pulse.

The maximal output power of the millimeter-wave source is on the order of tens of milliwatts [10]. The transition-dipole matrix elements for transitions between Rydberg states scale as n^2 so that the output power had to be lowered to its minimum in order to avoid saturation broadening of the investigated transitions. The intensity of the millimeter-wave radiation interacting with the atoms had to be further reduced by placing a stack of 500 sheets of paper between the source and the atom cloud. This measure effectively blocked the direct optical path, and the transitions were induced by reflected or scattered radiation. Under these conditions, the intensity was low enough to avoid saturation broadening, which enabled us to fully exploit the narrow bandwidth of the millimeter-wave source. However, the polarization of the millimeter-wave radiation interacting with the Rydberg atoms was not well defined.

B. Detection of the Rydberg atoms

The Rydberg atoms were detected by monitoring the field-ionization signal induced by a slowly rising negative potential U_{ion} applied to all ring electrodes and the grid in front of the MCP over a simple RC low-pass filter ($R = 8.2$ kΩ, $C =$ 100 pF). The resulting field selectively ionized all Rydberg states in the volume of the MOT and extracted the positively charged Cs^+ ions towards the MCP detector. The time-of-flight traces were read out by an oscilloscope and processed further using a LabView program. U_{ion} was adjusted to the n values of the investigated Rydberg states such that initial and final Rydberg states appeared as separate signals in the time-of-flight traces. All timings relevant for Rydberg state excitation and detection were controlled by a high-precision delay generator (Quantum Composer 9528). To reduce the

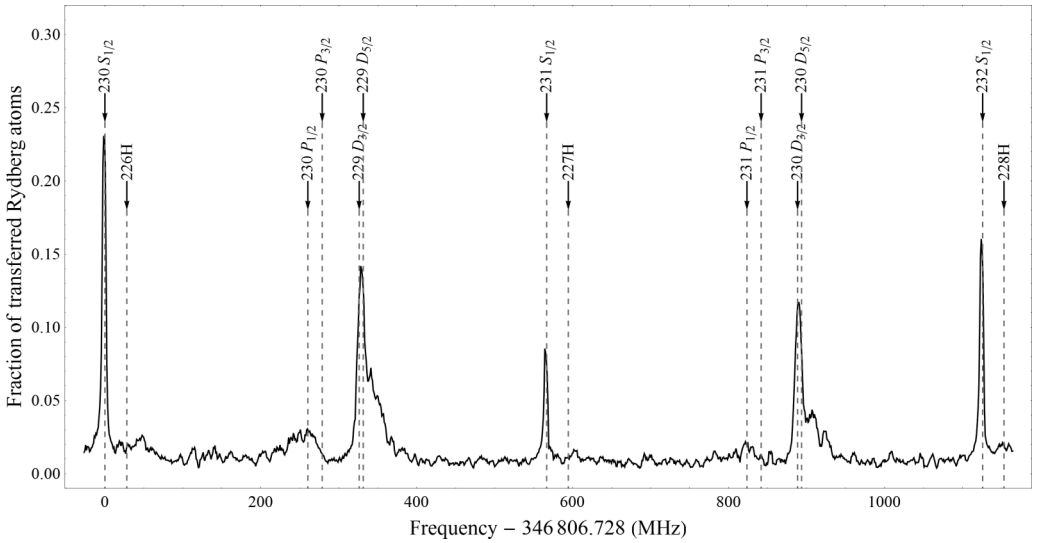

FIG. 4. Millimeter-wave spectrum of Rydberg states around $231S_{1/2}$ excited from the initial $93P_{3/2}$ state. The dashed vertical lines are calculated line positions based on the extrapolated quantum defects of Ref. [9]. The appearance of the dipole-forbidden transitions $nP_{1/2,3/2} \leftarrow 93P_{3/2}$ and the apparent line broadening are caused by the residual electric fields.

effects of shot-to-shot intensity and frequency fluctuations of the UV laser, the field-ionization signal of the final state of the transitions was normalized to the total ion yield. At low number densities of excited atoms, this ratio is independent of the absolute number of excited Rydberg atoms. To increase the signal-to-noise ratio, the signal of 80 experimental cycles was averaged at each spectral position.

C. Measurement and compensation of stray fields

Stray electric fields were compensated by applying potentials to the field plates described in Sec. II B (see Figs. 2 and 3). The voltages were applied to the electrodes such that the electric potential at the position of the MOT remains zero. By changing the polarity and the magnitude of these three potentials, any homogeneous electric field can be generated in the central region of the electrodes.

The compensation fields were optimized by minimizing the Stark shifts of $n'S_{1/2} \leftarrow nP_{3/2}$ transitions recorded with the millimeter-wave radiation. Because the states experience a quadratic Stark effect at low field strengths, the stray field can be compensated in each spatial dimension independently. First, a rough compensation of the stray field was performed at low n values. Then the procedure was repeated at progressively higher n values, exploiting the increasing sensitivity to stray fields resulting from the n^7 scaling of the polarizability [2]. In Fig. 4 a millimeter-wave spectrum of transitions from the $93P_{3/2}$ state to well-resolved Rydberg states with $n \sim 230$ is shown. At such high n values, the line widths could not be reduced by varying the voltages applied to the compensation electrodes and were found to be independent of the ground- and Rydberg-state density. The line widths increased, however, with increasing polarizabilities of the coupled states. Consequently, the line broadening is attributed to an electric field gradient originating from the residual stray field or from ions embedded in the atom cloud. Ions could result from collisions of Rydberg atoms, from blackbody-induced ionization, and from two-photon ionization of ground-state atoms by combination of a UV photon and an IR photon (all IR beams are turned off by AOMs, but a small amount of light can leak through). From the experimental line width of ≈2 MHz for the $230S_{1/2} \leftarrow 93P_{3/2}$ transition and calculated Stark shifts of the Rydberg states involved, it can be excluded that the residual electric stray field varies by more than 1 mV/cm over the atomic sample. Thus, initial stray fields of about 250 mV/cm could be reduced to less than 1 mV/cm. The spectrum displayed in Fig. 4 illustrates the possibility to fully resolve Rydberg states of very high principal quantum numbers.

The magnetic stray field was compensated using the three pairs of magnetic coils described in Sec. II C. Rydberg atoms undergo a linear Zeeman effect in a magnetic field. Consequently, the components of the magnetic stray field along the different axes cannot be compensated independently, which complicates the stray-field compensation procedure.

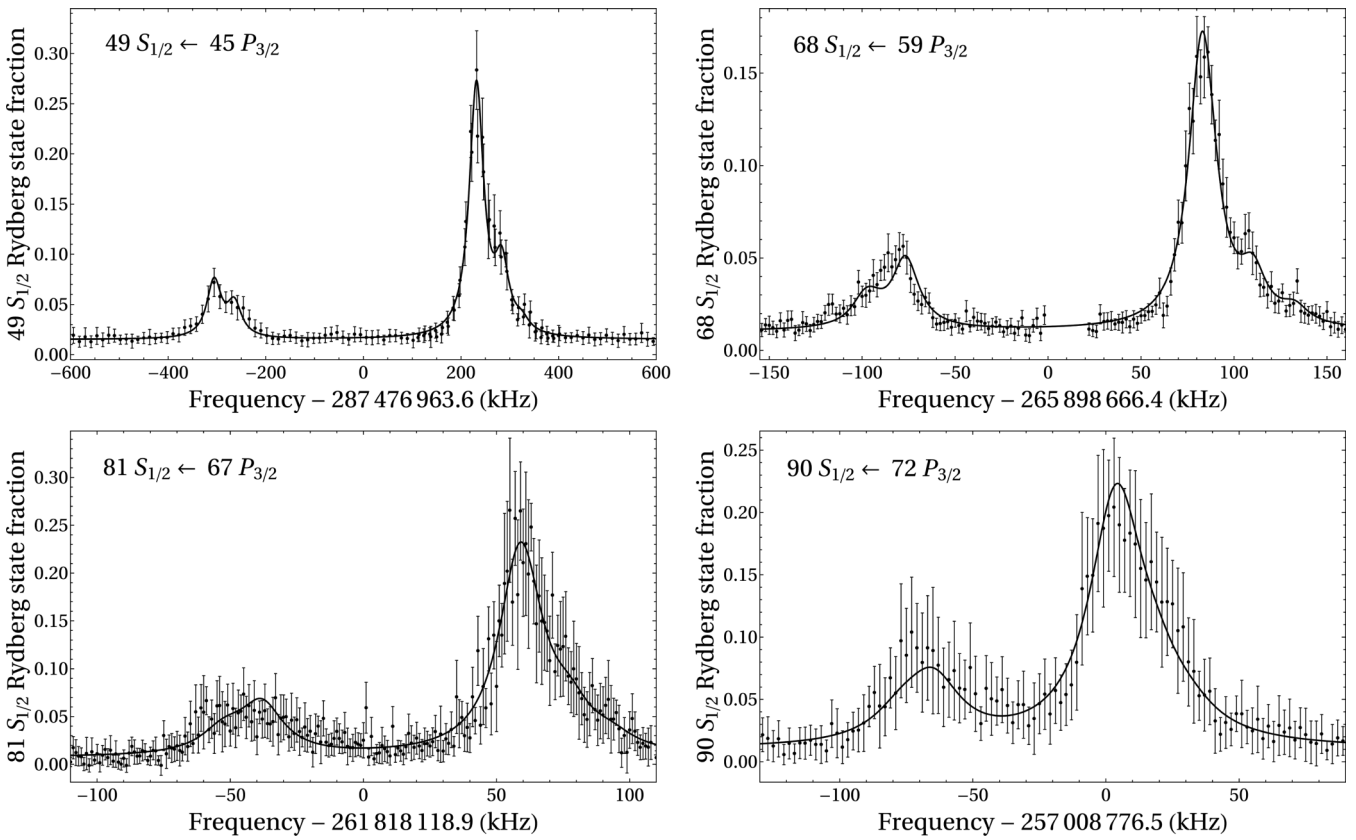

FIG. 5. Experimental and simulated spectra of millimeter-wave transitions between $nP_{3/2}$ and $n'S_{1/2}$ Rydberg states of cesium ($49S_{1/2} \leftarrow 45P_{3/2}$, $68S_{1/2} \leftarrow 59P_{3/2}$, $81S_{1/2} \leftarrow 67P_{3/2}$, $90S_{1/2} \leftarrow 72P_{3/2}$). Each point represents an average over 80 laser shots. The error bars show the standard deviation of each measurement. The black line is a simulated spectrum that has been fitted according to the model described in the Appendix.

We first exploited the mechanical Hanle effect [20] for a coarse compensation of the magnetic field in two directions: an additional laser beam, resonant with the transition $6P_{3/2}, F' = 4 \leftarrow 6S_{1/2}, F = 4$ and circularly polarized, was passed through the atom cloud in x direction (see Fig. 2). By applying a magnetic field of up to 100 mG in the x direction a quantization axis was defined for the total angular momentum $\vec{F}$ of the atoms. If the magnetic-field components perpendicular to this axis are significantly smaller than the quantization field, the circular polarized light drives predominantly $\sigma^{+/-}$ transitions and thus optically pumps the atoms into one of the maximally oriented states $F = 4, m_F = \pm 4$, which are dark states in this configuration. Thus every atom scatters only few photons before decoupling from the light field. Any component of the magnetic field perpendicular to the quantization axis weakens the efficiency of the dark-state pumping, because π transitions become allowed. In this case, every atom scatters photons continuously and thus experiences a mechanical force in the direction of the laser beam, resulting in a displacement of the atom cloud. We observe this displacement by imaging the fluorescence of the cloud on a CCD camera and compensate for stray magnetic fields in the y and z directions by reducing the observed displacement while varying the current applied to the compensation coils. Then the remaining magnetic stray field was compensated by measuring the Zeeman effect in millimeter-wave spectra. In this way, initial magnetic stray fields of about 550 mG could be reduced first to approximately 70 mG using the mechanical Hanle effect and further to below 2 mG using millimeter-wave spectroscopy. The latter value was estimated by comparing spectra calculated for different magnetic-field strengths to experimental millimeter-wave spectra (see next section) and is limited by the accuracy of 1 mA with which the currents applied to the compensation coils can be adjusted.

IV. MEASUREMENT OF THE HYPERFINE STRUCTURE OF RYDBERG STATES

Stray electric and magnetic fields below 1 mV/cm and 2 mG, respectively, have almost no detectable effect on Rydberg states with $n < 100$ at our resolution. Consequently, the hyperfine structure of high-lying Rydberg states could be investigated with high precision. Exemplary millimeter-wave spectra of $n'S_{1/2} \leftarrow nP_{3/2}$ transitions are shown in Fig. 5. The hyperfine splitting of the $F = 3$ and $F = 4$ components of the $nS_{1/2}$ states is clearly resolved in these spectra for n up to 90. The two components are broadened by the hyperfine structure of the initial $nP_{3/2}$ state, which is only partially resolved for $n \gtrsim 70$.

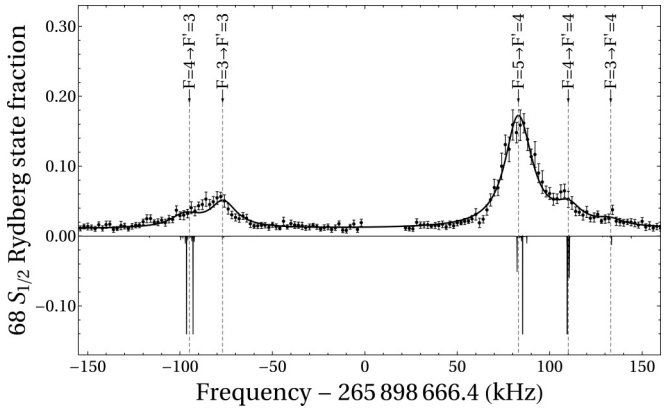

FIG. 6. Millimeter-wave spectrum of the $68S_{1/2} \leftarrow 59P_{3/2}$ transition including a fitted simulation (thick black line) and an assignment of the single hyperfine transitions (black arrows on dashed vertical lines). The inverted stick spectrum, on which the simulation is based, is presented in arbitrary intensity units and shows the splitting of the $F' \leftarrow F$ transitions into their M_F components at the residual magnetic field of 2 mG.

The experimental spectra could be modeled accurately by taking into account the hyperfine and the Zeeman interactions of initial and final states, and a finite Lorentzian line profile. The model used for the calculation of spectra is described in detail in the Appendix. The adjustment of the calculated to the measured spectra allowed us to determine the spectral resolution, the hyperfine coupling constants of the states involved, and the initial polarization of the atomic sample. As an example, the experimental spectrum of the $68S_{1/2} \leftarrow 59P_{3/2}$ transition is compared to a spectrum calculated with the adjusted model and an assignment of the different spectral

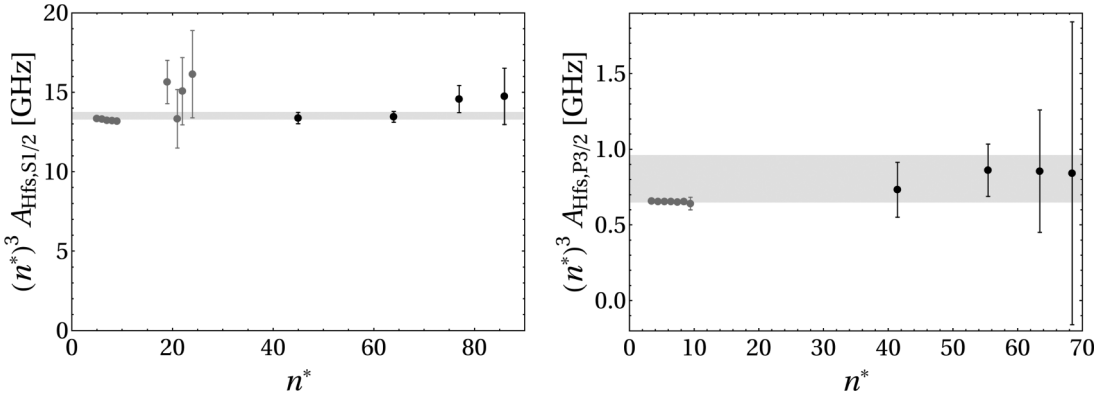

FIG. 7. Plot of the fitted magnetic dipole constants of the hyperfine structure of $nS_{1/2}$ (a) and $nP_{3/2}$ (b) Rydberg states of cesium atoms weighted by $(n^*)^3$ vs n^* (our measurements are shown in black). The gray bar represents the 95% confidence interval of a weighted average of all four measurements and guides the eye for the comparison with the literature data [9,22–29] (shown in gray) at lower principal quantum numbers.

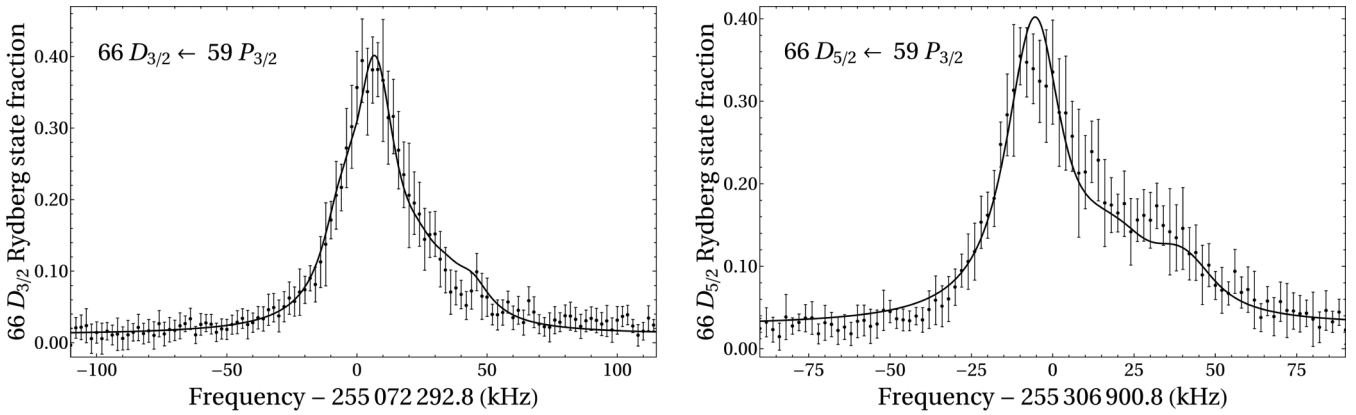

FIG. 8. Experimental and simulated spectra of millimeter-wave transitions from the $59P_{3/2}$ Rydberg state to the $66D_{3/2}$ and $66D_{5/2}$ states of cesium.

features in Fig. 6. From the adjusted model, we obtain a line profile with a full width at half maximum (FWHM) of 17(3) kHz. This is in good agreement with the convolution of the Fourier transform of the 60 μs long millimeter-wave pulse and a lifetime-limited atomic line width of 2.5 kHz [21], yielding a FWHM of 17.0 kHz. The experimental line width increases to 19(3) kHz and 24(3) kHz for the millimeter-wave spectra of the transitions to the $81S_{1/2}$ and $90S_{1/2}$ states, respectively. This is in qualitative agreement with a Stark broadening caused by a residual electric field gradient of 100 mV/cm^2.

For each spectrum depicted in Fig. 5, the magnetic dipole hyperfine coupling constant $A_{\mathrm{hfs},P_{3/2}}$ of the $nP_{3/2}$ states was obtained by adjusting the model to the two hyperfine components of the $nS_{1/2}$ state separately. The magnetic dipole constant $A_{\mathrm{hfs},S_{1/2}}$ of the $nS_{1/2}$ state was then obtained in a second step by leaving $A_{\mathrm{hfs},P_{3/2}}$ unchanged and fitting the overall amplitude and frequency shift of the model to the complete experimental spectrum. The hyperfine coupling constants of these high Rydberg states can be compared to reported values measured at lower principal quantum numbers [9,22–29]. The hyperfine structure results from the Fermi contact interaction of the Rydberg electron with the nucleus and is therefore proportional to the probability density of the Rydberg electron at the nucleus. It scales with $(n^*)^{-3}$, where $n^* = n - \delta_\ell$ is the effective principal quantum number and δ_ℓ is the ℓ-dependent quantum defect. One can thus introduce a reduced hyperfine coupling constant $A^*_{\mathrm{hfs},\ell}$ as $A_{\mathrm{hfs,n^*},\ell} = \frac{A^*_{\mathrm{hfs},\ell}}{n^{*3}}$. The so-obtained reduced coupling constants were compared to previously published values [9,22–29] in Fig. 7 (quantum defects are taken from Ref. [9]). Because the hyperfine structure of the $nP_{3/2}$ states could not be resolved, the magnetic dipole coupling constants of the $nP_{3/2}$ states were deduced only from the line shape and line width and are therefore associated with larger uncertainties, whereas the hyperfine coupling constants of the $nS_{1/2}$ states could be determined with an accuracy comparable to, or exceeding the accuracy of the measurements at low n^*. The weighted averages of the reduced coupling parameters for both $nP_{3/2}$ and $nS_{1/2}$ states are $A^*_{\mathrm{hfs,P_{3/2}}} = 0.80(8)$ GHz and $A^*_{\mathrm{hfs,S_{1/2}}} = 13.53(12)$ GHz, respectively. For $A^*_{\mathrm{hfs},P_{3/2}}$, we obtain systematically higher values than previously reported for lower n values. The discrepancy could be the result of line-broadening effects by the residual electric field and the gradients of both electric and magnetic fields, which are not included in our model.

The modeled line shapes are sensitive to the initial population of M_F states in the $6s^2S_{1/2}, F = 4$ ground state, i.e., to the orientation of the initial atomic sample before Rydberg excitation. Experimentally, we polarize the sample by applying a circular polarized pump laser pulse, which is switched off 20 μs before the excitation to Rydberg states (see Sec. III A). In the model, the initial polarization was treated as a global parameter being constant for all spectra presented in Figs. 5, 6, and 8. The optimal agreement with the experimental spectra was obtained assuming that 95% of the atoms remain in the $M_F = 4$ component until excitation to Rydberg states. The timescale for depolarization is limited in our experiment by the precession of the magnetic moment of the cesium atoms around the axis of the stray magnetic field with the Larmor period $T_L = (\frac{\mu_B g_F B_{\mathrm{res}}}{h})^{-1}$, where μ_B is the Bohr magneton, and $g_F = 1/4$ the g factor of the $6S_{1/2}, F = 4$ state. By taking a value of $B_{\mathrm{res}} = 2$ mG for the residual magnetic field, we obtain $T_L = 1.4$ ms, which explains why we do not observe a significant depolarization of the atomic sample during the 20 μs delay between optical pumping and Rydberg excitation.

We also recorded spectra of transitions from the $59P_{3/2}$ state to the $66D_{3/2}$ and $66D_{5/2}$ states, which are depicted in Fig. 8. The asymmetric line profiles result from the combined hyperfine structure of the initial and final states, which is not resolved. However, because we have independently determined the hyperfine coupling constant of the $59P_{3/2}$ state, we can extract the hyperfine coupling constants of $A_{\mathrm{hfs,66D_{3/2}}} = 2.6(5)$ kHz and $A_{\mathrm{hfs,66D_{5/2}}} = 0.10(45)$ kHz for the D states.

V. CONCLUSION

An experimental setup for high-resolution spectroscopy of cesium Rydberg states has been presented. Its performance was demonstrated by the measurement of the hyperfine structure of $nS_{1/2}$ states at $n = 45$–90 using millimeter-wave spectroscopy and the excitation of very-high-n Rydberg states with $n = 230$ in the noninteracting regime (low ground- and Rydberg-state

density). For $n < 100$, the hyperfine splitting of the $nS_{1/2}$ Rydberg states could be resolved in the measured millimeter-wave spectra. From the modeling of the experimental spectra, magnetic dipole coupling constants for the hyperfine structure of the $nS_{1/2}$ and $nP_{3/2}$ states were obtained which are in agreement with measurements at lower n values. To achieve the required resolution, electric and magnetic stray fields of 250 mV/cm and 560 mG had to be compensated so that the residual fields were below 1 mV/cm and 2 mG, respectively. Our experiments exploited the fact that the factors that usually limit the resolution of spectroscopic measurements are negligible in our setup. Indeed, the Doppler broadening is well below 1 kHz in samples of ultracold atoms at low frequencies. Moreover, the low temperature of the atomic sample enables measurement times extending beyond 100 μs. The control over the stray electric and magnetic fields demonstrated in this article was essential for the determination of the hyperfine structure of Rydberg states of Cs at high n values and to retain a full coherence and avoid a significant depolarization of the atomic sample over a time scale of up to 60 μs.

APPENDIX: CALCULATION OF SPECTRA

The simulation of the experimental spectra requires the calculation of line positions and line intensities and a convolution with the instrumental line profile. In order to calculate the line positions, the energies of the hyperfine levels in a magnetic field of the initial and the final Rydberg state are obtained by diagonalizing the Hamiltonian matrix [8]

$$\hat{H} = \hat{H}_{\rm hfs} + \hat{H}_{\rm Z} = A_{\rm hfs}(\hat{\vec{I}} \cdot \hat{\vec{J}}) + g_J \mu_{\rm B} B_z \hat{J}_z. \qquad \text{(A1)}$$

The Hamiltonian consists of the hyperfine-structure Hamiltonian $\hat{H}_{\rm hfs}$ in the magnetic dipole approximation and the Zeeman Hamiltonian $\hat{H}_{\rm Z}$ for the electron spin. Neglecting the Zeeman effect of the nuclear spin is justified because the electron g factor is three orders of magnitude larger than the g factor of the nucleus. Neglecting higher multipoles in $\hat{H}_{\rm hfs}$ is also justified, because the magnetic quadrupole constant of Cs is two orders of magnitude smaller than the magnetic dipole constant [30]. The Hamiltonian matrix is evaluated in the $|F, M_F\rangle$ basis, in which $\hat{H}_{\rm hfs}$ is diagonal, with matrix elements

$$\langle F|\hat{H}_{\rm hfs}|F\rangle = \tfrac{1}{2} A_{\rm hfs}[F(F+1) - I(I+1) - J(J+1)]. \qquad \text{(A2)}$$

The Zeeman Hamiltonian $\hat{H}_{\rm Z}$ is diagonal in the basis of $|I, M_I, J, M_J\rangle$, and the matrix elements in this basis are given by

$$\langle I, M_I, J, M_J|\hat{H}_{\rm Z}|I, M_I, J, M_J\rangle = g_J \mu_{\rm B} B_z M_J, \qquad \text{(A3)}$$

where the Landé g factor was taken as $g_J = 1 + \frac{J(J+1)+S(S+1)-L(L+1)}{2J(J+1)}$ [31]. The basis transformation from the $|I, M_I, J, M_J\rangle$ to the $|F, M_F\rangle$ basis was then applied to $\hat{H}_{\rm Z}$, the resulting matrix was added to $\hat{H}_{\rm hfs}$, and the total Hamiltonian matrix was numerically diagonalized. The transition frequencies were obtained as differences between the eigenenergies of the final and initial states.

For the calculation of the line intensities, the initial distribution of M_F levels in the $F = 4$ hyperfine component of the $6S_{1/2}$ state of cesium and the ΔM_F selection rules for both Rydberg excitation and Rydberg-Rydberg transitions were taken into account. The UV laser is linearly polarized with its polarization axis perpendicular to the quantization axis of the atoms after optical pumping. Consequently the UV laser drives $\Delta M_F = \pm 1$ transitions. The polarization of the millimeter-wave radiation interacting with the cesium atoms was not controlled in the experiments, and the ratio of $\Delta M_F = \pm 1$ to $\Delta M_F = 0$ transitions has been determined empirically in a global analysis of all spectra. A ratio of 70% $\Delta M_F = 0$ and 30% $\Delta M_F = \pm 1$ yielded best overall agreement with the experimental results. This ratio was kept unchanged in the simulation of all spectra presented in Figs. 5, 6, and 8. The transition strengths could then be evaluated using the spherical angular-momentum dipole matrix elements

$$\begin{aligned}\langle F M_F|er_q|F' M_F'\rangle &= \langle J||e\mathbf{r}||J'\rangle (-1)^{2F'+J+M_F+I}\sqrt{(2F+1)(2F'+1)(2J+1)} \\ &\times \begin{pmatrix} F' & 1 & F \\ M_F' & q & -M_F \end{pmatrix} \begin{Bmatrix} J & J' & 1 \\ F' & F & I \end{Bmatrix}. \end{aligned} \qquad \text{(A4)}$$

Because only the relative transition strength between the different $|F, M_F\rangle$ levels is observable in the experimental spectra, and the reduced matrix element $\langle J||e\mathbf{r}||J'\rangle$ gives a constant contribution for all transitions with given $\Delta l = 1$ and $\Delta J = 0, 1$ values, this term was not evaluated in the calculation of the transition dipole moments. The line intensities were obtained as the product of the relative population in a given M_F level of the $P_{3/2}$ Rydberg state and the spherical matrix elements for the transitions to the S and D states. For calculations including a nonzero magnetic field, the line intensities were further weighted by the admixture of initial and final states (in the unperturbed $|F, M_F\rangle$ basis) to the eigenstates of $\hat{H}$ in the magnetic field. The magnitude of the residual magnetic field was treated as a global fit parameter. The best agreement between experimental spectra and simulation was obtained for a residual magnetic field of 2 mG.

The convolution of the Fourier transform of the square excitation pulse (a sinc function) and the Lorentzian line profile of the atomic transition was found to be adequately described by a Lorentzian line profile. Thus the stick spectra obtained with the calculated line positions and intensities were convoluted with this line-profile function. The overall amplitude and an arbitrary frequency shift of the resulting spectra were fitted separately to each experimental spectrum, as well as the magnetic dipole constants of the initial and final state and the Lorentzian line width.

[1] H. A. Bethe and E. E. Salpeter, *Quantum Mechanics of One- and Two-Electron Atoms* (Springer, Berlin, 1957).

[2] T. F. Gallagher, *Rydberg Atoms* (Cambridge University Press, Cambridge, 2005).

[3] A. Osterwalder and F. Merkt, Phys. Rev. Lett. **82**, 1831 (1999).

[4] T. Vogt, M. Viteau, A. Chotia, J. Zhao, D. Comparat, and P. Pillet, Phys. Rev. Lett. **99**, 073002 (2007).

[5] M. S. O'Sullivan and B. P. Stoicheff, Can. J. Phys. **61**, 940 (1983).
[6] C.-J. Lorenzen and K. Niemax, Z. Phys. A **315**, 127 (1984).
[7] K.-H. Weber and C. J. Sansonetti, Phys. Rev. A **35**, 4650 (1987).
[8] E. Arimondo, M. Inguscio, and P. Violino, Rev. Mod. Phys. **49**, 31 (1977).
[9] P. Goy, J. M. Raimond, G. Vitrant, and S. Haroche, Phys. Rev. A **26**, 2733 (1982).
[10] M. Schäfer, M. Andrist, H. Schmutz, F. Lewen, G. Winnewisser, and F. Merkt, J. Phys. B **39**, 831 (2006).
[11] M. T. Frey, X. Ling, B. G. Lindsay, K. A. Smith, and F. B. Dunning, Rev. Sci. Instrum. **64**, 3649 (1993).
[12] D. Klar, M. W. Ruf, and H. Hotop, Meas. Sci. Technol. **5**, 1248 (1994).
[13] E. Urban, T. A. Johnson, T. Henage, L. Isenhower, D. D. Yavuz, T. G. Walker, and M. Saffman, Nat. Phys. **5**, 110 (2009).
[14] A. Gaëtan, Y. Miroshnychenko, T. Wilk, A. Chotia, M. Viteau, D. Comparat, P. Pillet, A. Browaeys, and P. Grangier, Nat. Phys. **5**, 115 (2009).
[15] T. Vogt, Ph.D. thesis, Université Paris-Sud 11, 2006.
[16] W. Li, I. Mourachko, M. W. Noel, and T. F. Gallagher, Phys. Rev. A **67**, 052502 (2003).
[17] G. C. Bjorklund, M. D. Levenson, W. Lenth, and C. Ortiz, Appl. Phys. B **32**, 145 (1983).
[18] B. P. Anderson and M. A. Kasevich, Phys. Rev. A **63**, 023404 (2001).
[19] J. M. Raimond, M. Gross, C. Fabre, S. Haroche, and H. H. Stroke, J. Phys. B **11**, L765 (1978).
[20] R. Kaiser, N. Vansteenkiste, A. Aspect, E. Arimondo, and C. Cohen-Tannoudji, Z. Phys. D **18**, 17 (1991).
[21] V. D. Ovsiannikov, I. L. Glukhov, and E. A. Nekipelov, J. Phys. B **44**, 195010 (2011).
[22] G. Belin, L. Holmgren, and S. Svanberg, Phys. Scr. **14**, 39 (1976).
[23] P. Tsekeris, J. Farley, and R. Gupta, Phys. Rev. A **11**, 2202 (1975).
[24] P. Tsekeris, R. Gupta, W. Happer, G. Belin, and S. Svanberg, Phys. Lett. A **48**, 101 (1974).
[25] G. Belin and S. Svanberg, Phys. Lett. A **47**, 5 (1974).
[26] S. Rydberg and S. Svanberg, Phys. Scr. **5**, 209 (1972).
[27] J. Farley, P. Tsekeris, and R. Gupta, Phys. Rev. A **15**, 1530 (1977).
[28] H. Bucka, H. Kopfermann, and E. W. Otten, Ann. Phys. **459**, 39 (1959).
[29] H. Bucka and G. von Oppen, Ann. Phys. **465**, 119 (1962).
[30] V. Gerginov, A. Derevianko, and C. E. Tanner, Phys. Rev. Lett. **91**, 072501 (2003).
[31] F. Schwabl, *Quantum Mechanics* (Springer, Berlin, 2007).